Characterizing spin-orbit coupling in materials using time-resolved Faraday rotation.

Trigg Randall

A senior thesis submitted to the faculty of
Brigham Young University
in partial fulfillment of the requirements for the degree of

Bachelor of Science

John Colton, Advisor

Department of Physics and Astronomy

Brigham Young University

ABSTRACT

Characterizing spin-orbit coupling in materials using time-resolved Faraday rotation.

Trigg Randall
Department of Physics and Astronomy, BYU
Bachelor of Science

Time-resolved Faraday rotation is an ultrafast pump-probe spectroscopy experiment which can characterize the spin properties of materials. To utilize materials in spintronics applications, it is essential to quantify the spin-orbit coupling and the spin lifetimes of potential materials. In particular, hybrid organic-inorganic perovskites have significant potential in spintronics devices due to their strong optoelectronic and spin properties. For instance, methylammonium lead iodide ($MAPbI_3$) has a strong spin-orbit coupling and abnormally long spin decoherence times. In this work, I design and set up a time-resolved Faraday rotation experiment. I demonstrate that it can accurately characterize the *g*-factor of a GaAs/AlGaAs heterostructure within experimental uncertainties. Furthermore, tests were conducted on $MAPbI_3$ that did not obtain expected results, but demonstrate promise for future measurements.

Keywords: time-resolved Faraday rotation, spin-orbit coupling, perovskite, exciton, spin relaxation

ACKNOWLEDGMENTS

I would like to thank my advisor John Colton for his continued support and guidance throughout this project. He has cultivated my passion and curiosity for my research and helped me solve the inevitable problems that arose. I would also like to thank my wife for her love and support throughout this work. Knowing that she is always there with me helped me get through the tough times when the work was frustratingly slow.

Contents

List of Figures

Chapter 1

Introduction

Since the 1960s, our expanding understanding of silicon has led to dramatic growth in computing power and technology, propelling humanity into the information age. Following Moore's law, the number of transistors on a single computer chip has approximately doubled every two years since the advent of silicon devices. Early computers were limited to calculation speeds on the order of 100 calculations per second; now, most commercial processors can perform up to 10^9 calculations per second. However, in the past decade, the limitation of silicon-based semiconductor devices has become apparent as device scaling for faster, more efficient computers becomes more difficult and expensive. Unique semiconductor materials offer alternative solutions to this problem through their integration in existing device architectures or the development of novel devices such as spin field-effect transistors (spinFETs) [1].

Spin field-effect transistors utilize the traditional MOSFET architecture, as shown in Figure 1.1. They work as an analog to using a polarizer/analyzer duo in tandem with some electro-optic material. Light will be polarized at some axis after passing through the first polarizer. If the analyzer is rotated 90° relative to the polarizer (assuming the electro-optic material has no residual birefringence), no light will be transmitted through the system. Now, applying a voltage across the electro-optic material will rotate the incident polarization. To maximize the transmitted light, a gate voltage is

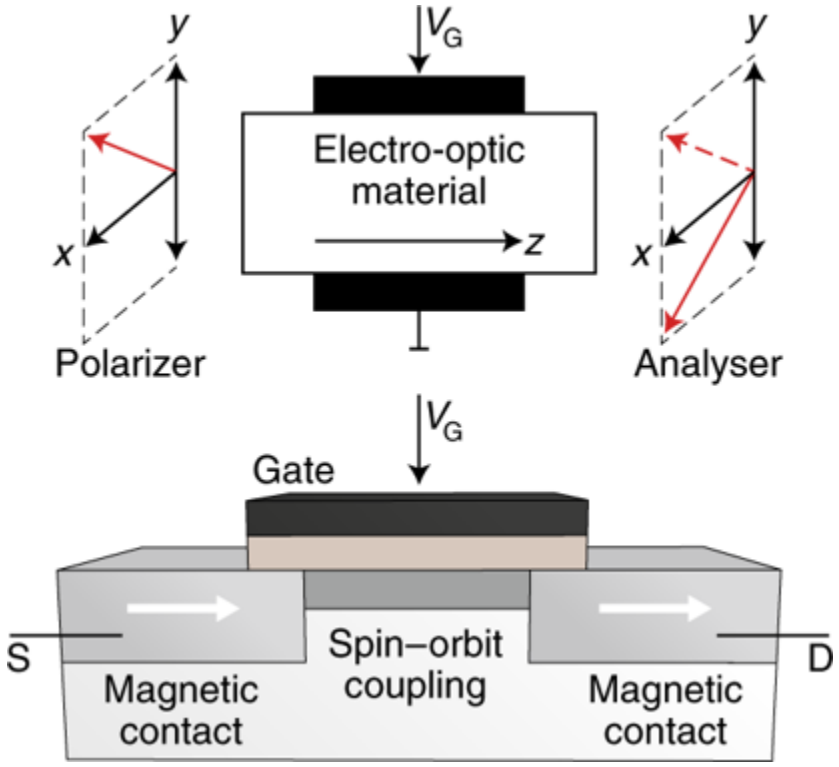

Figure 1.1 Comparison between an electro-optic modulator and proposed architecture for a spin field-effect transistor. The bulk substrate is a semiconductor with large spin-orbit coupling, connected to magnetic source and drain contacts. The spin-orbit coupling strength is tuned using an externally applied gate voltage V_G, which rotates the spins of electrons transmitted through the material. Figure taken from [2].

applied that causes the incident light to rotate 90° so none of the incident light is lost when it goes through the analyzer.

The spinFET utilizes the same principle to control whether a device is on (has low resistance) or off (has high resistance) [2]. The ferromagnetic source and drain contacts are magnetized 180° relative to each other—instead of 90° in the photon polarizer analogy. The first contact injects spin-up electrons into the semiconductor channel. If the electron spins remain constant in the channel, then the second contact will act as a spin filter and completely block the current. However, if the electron spins rotate to align with the magnetization vector of the second contact, they will be transmitted. Similar to the electro-optic comparison, a gate voltage can tune the spin-orbit coupling of the semiconducting substrate, which allows one to control the electron spin rotation to maximize or minimize the transmitted current.

Replacing the traditional MOSFET architecture with the spinFET architecture can improve operating speeds and reduce power losses. However, only materials with specific spin properties are suitable for this application. For instance, semiconductors such as InAlAs, InAs, and InGaAs with suitable spin-orbit coupling have been used as the channel material for those devices by creating a two-dimensional electron gas in a quantum well heterostructure [3], but each material introduces sub-optimal qualities. Mainstream use of the spinFET is still restricted because of limited scalability—since indium-based III-V semiconductors are typically synthesized using molecular beam epitaxy, which is difficult to use in large-scale operations—and architectural limitations for devices that operate at room temperature (the channel length must be short for device operations at high temperatures) [4]. To address these issues, we must investigate alternative semiconductor materials to replace the indium-based III-V channel materials.

1.1 Hybrid Organic-Inorganic Perovskites

Perovskite semiconductors have made waves in the scientific community recently because they can be synthesized using scalable methods and they exhibit a large degree of tunability. The original perovskite, discovered in 1839, was calcium titanate ($CaTiO_3$). Most perovskite structures follow the formula ABX_3, where A and B are cations and X is an anion. By substituting various cations in place of A or B or anions in place of X, new compounds can be reliably synthesized with different characteristics. For instance, the material can develop new phases when a heavy cation replaces B or a halide replaces X. Likewise, the band gap (E_g) and exciton binding energy, among other electronic properties, can be tuned this way. Furthermore, the dimensionality of such samples can be controlled by implementing large organic cations in place of A to push inorganic layers apart into two-dimensional (2D) sheets.

Hybrid organic–inorganic perovskites (HOIPs) are a novel development in perovskite materials. The prototypical HOIP, methylammonium lead iodide ($MAPbI_3$), has been extensively studied due to its band gap of 1.5–1.6 eV at room temperature—which corresponds to a 30%–32% maximum solar conversion efficiency by the Shockley-Queisser limit—large spin-orbit coupling (SOC), and light-emitting capabilities. By substituting different molecules and atoms into the structure, characteristic properties, including the band gap and exciton binding energy, change in a predictable way. Furthermore, slightly altering parameters in the synthesis process can allow significant control over these properties.

Figure 1.2 shows the unit cell for $MAPbI_3$. The PbI_6^- inorganic octahedra form a cubic structure, with the space in the middle of the cube filled by the organic MA^+ cation.

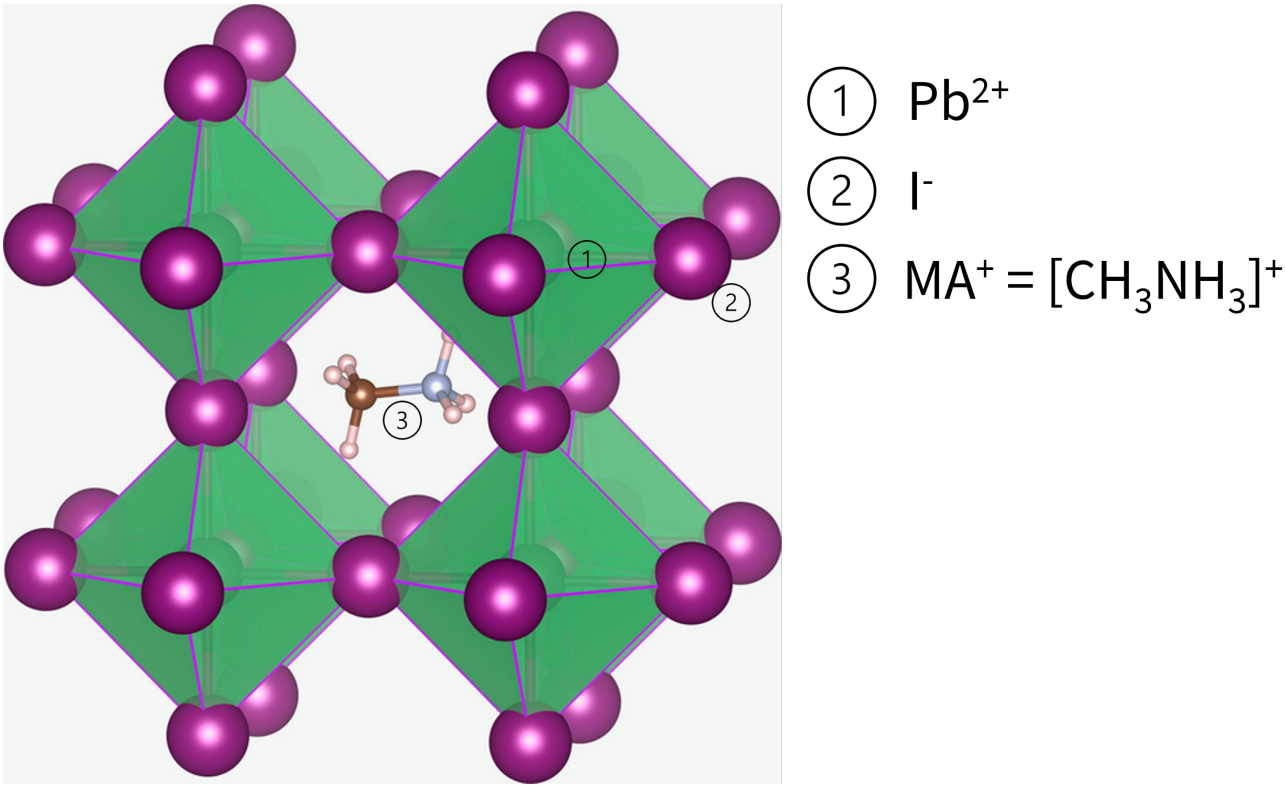

Figure 1.2 Structure of methylammonium lead iodide crystal structure. The material forms inorganic octahedra composed of Pb^{2+} and I^-, with the organic MA^+ cations interspersed in the gap enclosed by the octahedra. Adapted from Eames et al. [5]

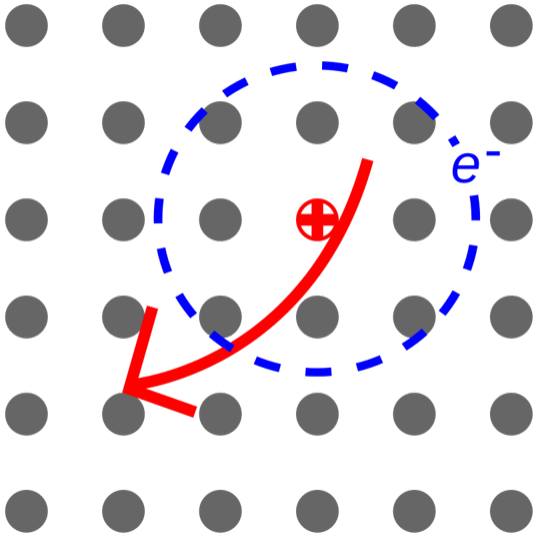

Figure 1.3 A classical picture of a Wannier-Mott exciton where the electron-hole pair are largely delocalized within the crystal. The effective Bohr radius of the exciton is large, corresponding to a weak binding energy. These excitons are typical in materials like $MAPbI_3$ with low exciton binding energies. Taken from Ref. [6].

1.1.1 Excitons

In semiconductor materials, certain photon energies below the band gap can still excite electrons into a new state. The electron motion correlates with a hole in the valence band such that they can be modeled like a hydrogen atom using the Bohr model, as seen in Figure 1.3. Depending on the material, the exciton motion can be localized or delocalized. The associated energy levels are depicted in Figure 1.4, where the E_{1s} exciton state is denoted $n = 1$, the E_{2s} exciton state is $n = 2$ and so on.

Excitons in semiconductors are associated with a binding energy. The exciton binding energy is the energy required to ionize the electron-hole pair such that the electron hops into the conduction band and the hole drops down to the valence band. In most cases, the larger the binding energy, the shorter the exciton's optical lifetime. At lower temperatures, the exciton lifetime is also larger (since thermal fluctuations contribute to excitonic decay). For instance, in GaAs, the exciton binding

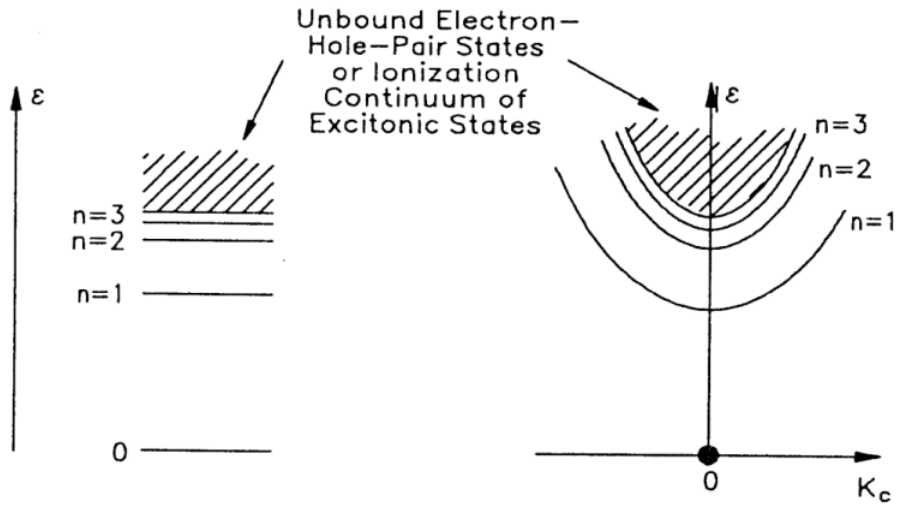

Figure 1.4 Excitonic energy levels imitate hydrogenic energy levels. They have discrete energies and populate energies close to the conduction band. The right picture depicts the dispersion relation for excitons as compared to the conduction band dispersion. Taken from Böer et al. [7].

energy is $E_b = 4.2$ meV [8], whereas the binding energy for unstrained $MAPbI_3$ is somewhere in the range of $E_b = 5$–13 meV at room temperature [9] [10] [11].

1.2 Spin-Orbit Coupling

Spin-orbit coupling arises from the relativistic Dirac equation in quantum mechanics [12]. Consider an electron orbiting a positively charged nucleus (a heavily classical but insightful view). As the electron circles the nucleus, it "carries" a current which generates a magnetic field in the center of its orbit. In the rest frame of the electron, the nucleus orbits the electron, generating an effective magnetic field B_{eff} at its position. This microscopic magnetic field interacts with the electron's spin magnetic moment. It splits the associated energies of spin-up vs. spin-down electrons—it is, effectively, an analog to Zeeman splitting for single-atom systems in an external magnetic field, lifting the electron spin degeneracy. In general, this causes what is known as the Pauli spin-orbit

interaction for single atoms. For a single electron, the Hamiltonian due to SOC is given by

$$H_{SOC} = \lambda \boldsymbol{\sigma} \cdot (\mathbf{k} \times \nabla U) \tag{1.1}$$

where λ is the SOC parameter, indicating the strength of the SOC, σ represents the Pauli spin matrices, and U is the electrostatic potential [13]. Thus, any asymmetric electrostatic potential which generates an electric field will cause spin-orbit interaction in solids.

The electric fields can be generated through various methods in solids. In **Rashba spin-orbit coupling**, the internal electric field arises due to structural inversion asymmetry (SIA) [12]. The Hamiltonian due to Rashba SOC is given by [13]

$$H_R = \alpha \, (\mathbf{p} \times \hat{\mathbf{z}}) \cdot \boldsymbol{\sigma}. \tag{1.2}$$

In a two-dimensional electron gas (2DEG), this will lift the spin degeneracy of the energy bands in $\mathbf{k}$-space, with energies given by [13]

$$E_{\mathbf{k}} = \frac{\hbar^2 k^2}{2m^*} \pm \alpha k \tag{1.3}$$

Both internal and external factors can contribute to the SIA in materials which exhibit large Rashba SOC. For instance, surface and defect states, where the translational symmetry of the crystal is broken, generate large Rashba SOC. For this reason, quantum well heterostructures (such as AlGaAs/GaAs) with thin (< 10 nm) GaAs well layers will exhibit large SOC. Furthermore, the strength of the Rashba SOC can be tuned externally by gating the material and applying an electrostatic potential at the interface.

In **Dresselhaus spin-orbit coupling**, the internal electric field arises due to bulk inversion asymmetry [12]. Thus, non-centrosymmetric materials—materials which lack an inversion center

in the unit cell—tend to exhibit Dresselhaus SOC. In particular, bulk zincblende structures—face-centered cubic structures which imitate the diamond structure but contain more than one atom type—such as GaAs or ZnS have large Dresselhaus SOC. The Hamiltonian for Dresselhaus SOC for a general cubic structure has the form [14]

$$\hat{H}_{3D} = \beta((k_x^2 - k_y^2)k_z\hat{J}_z + (k_z^2 - k_x^2)k_y\hat{J}_y + (k_y^2 - k_z^2)k_x\hat{J}_x) \tag{1.4}$$

where $\hat{J}$ is the total angular momentum operator and β is the Dresselhaus coupling factor. This is cubic in k, but for heterostructures oriented in the (001) plane, this can be simplified to [12]

$$\hat{H}_{2D} = \beta\langle k_z^2\rangle(\sigma_y k_y - \sigma_x k_x), \tag{1.5}$$

which is linear in the in-plane k vector. This lifts the spin degeneracy for electrons for identical k. Figure 1.5 depicts the direction for the effective magnetic field as seen by electrons at the Fermi surface for both Rashba and Dresselhaus effects.

Generally, both Rashba and Dresselhaus spin-orbit coupling are present in HOIPs such as $MAPbI_3$, where inversion symmetry is broken.

1.3 Spin Relaxation

To optimize materials for spintronics devices, it is integral to understand carrier spin relaxation. Fast spin relaxation in conduction electrons reduces the spin polarization too rapidly. For instance, for electrons traveling through a channel in a spinFET device, if the spins relax between the source and drain, the ferromagnetic contacts will not filter the spin states, and the device will not switch properly. Thus, both spin-orbit coupling and spin relaxation times must be optimized to maximize device efficiency. However, most materials with a large SOC also exhibit short spin relaxation times

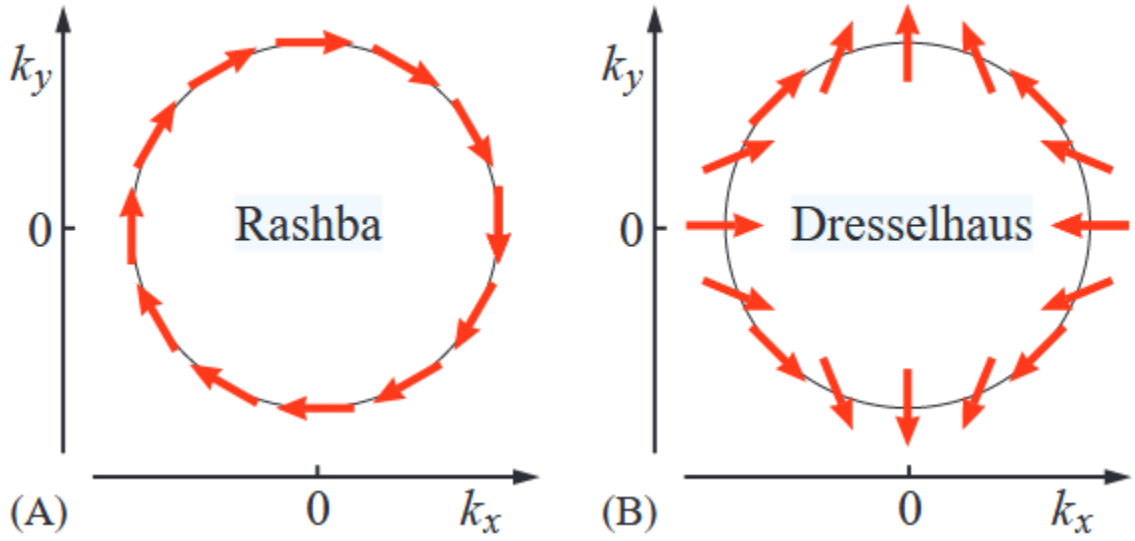

Figure 1.5 The effective magnetic field directions induced by (A) Rashba and (B) Dresselhaus are depicted for the Fermi surface in two dimensions. Adapted from [12].

on the order of femtoseconds, so finding a material which balances a large SOC effect and a long spin relaxation time is difficult. $MAPbI_3$ displays remarkably long spin relaxation times despite its large spin-orbit coupling [15]. Hence, it is a promising candidate to replace other semiconductor materials in spintronic devices.

In this paper, I design and set up a pump-probe time-resolved Faraday/Kerr rotation experiment. As a proof of concept, I first demonstrate that I can take accurate data on GaAs with the setup in Kerr (reflection) geometry. Then, I show measurements on $MAPbI_3$ samples with the setup in Faraday (transmission) geometry. In Chapter 2, I explain the experimental setup in both geometries. In Chapter 3, I demonstrate great agreement with previous data on GaAs and display data on $MAPbI_3$. In Chapter 4, future plans and possible solutions to obtaining accurate data on $MAPbI_3$ are given.

Chapter 2

Methods

2.1 Materials

During the course of this experiment, I measured results on *n*-GaAs and $MAPbI_3$. The GaAs sample consists of a *n*-GaAs/AlGaAs heterostructure with a doping concentration of 3×10^{15} cm^{-3}. It was grown via molecular beam epitaxy at the Naval Research Laboratory. More synthesis details are contained in Ref. [16].

Methylammonium lead iodide is typically synthesized by mixing a methylammonium iodide (MAI) and lead iodide (PbI_2) precursor solution. The solution is spin-coated on the substrate, forming thin films which are about 100-300 nm thick. The thin film and substrate are annealed at 100°C for 10 minutes and subsequently cooled to 25°C. The samples measured in this paper were synthesized by Kelsey Garden at the University of Utah.

2.2 Time-Resolved Faraday/Kerr Rotation

Time-resolved Faraday/Kerr rotation (TRFR/TRKR) is a pump-probe laser spectroscopy technique that uses spin-polarized carriers or excitons to measure a material's spin properties. The pump beam

is circularly polarized prior to hitting the material. Tuned to the excitonic peak of the sample, the pump excites electrons to form excitons. If the light incident on the sample is unpolarized, the spins of the resulting excitons will be purely random, such that the net magnetic moment of the material will average to 0. However, circularly polarized photons have spin ± 1. Optical selection rules require that spin angular momentum is conserved during optical transitions. For $MAPbI_3$, electrons in both the conduction band (CB) and valence band (VB) can only have spin $\pm\frac{1}{2}$. Thus, right circularly polarized (RCP) photons can only excite spin-down electrons to a spin-up state in the CB, while left circularly polarized (LCP) photons can only excite spin-up electrons to a spin-down state in the CB, as seen in Figure 2.1. The holes generated in the VB have the same spin as the electrons generated in the CB. Thus, the excitons formed by the resulting electron-hole pair have either spin +1 when excited by RCP photons or spin -1 when excited by LCP photons. Using these rules, I excite one spin state preferentially, resulting in a net spin polarization and a global magnetic moment in the material.

The probe beam is a linearly polarized beam which analyzes the spin polarization of the sample. During experimental setup, the path lengths of the pump and probe beam are controlled such that the probe travels further than the pump beam. That means that the probe pulse hits the sample slightly after the pump pulse. The spin polarization of the sample causes the index of refraction for RCP and LCP light to differ; thus, since linearly polarized light is a linear combination of RCP and LCP, one component receives a phase shift relative to the other. This phase shift results in a rotation of the linearly polarized probe pulse. The amount of rotation is proportional to the strength of the carrier spin orientation in the material. This is detailed in Figure 2.2 below.

After the material is spin polarized, the system gradually returns to its equilibrium state as the aligned spins decay into random ordering. One can measure the decay of the material's spin orientation by adjusting the time delay between the pump and probe beams. Using a delay stage, the path length of the pump is altered. Then, for a given path length, the probe is incident on the

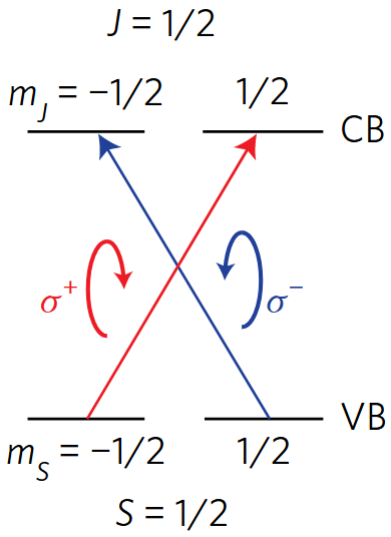

Figure 2.1 Optical selection rules for electrons in $MAPbI_3$. Electrons in the valence and conduction bands can only have spin $\pm\frac{1}{2}$. Circularly polarized photons have spin ± 1. Thus, RCP photons only excite spin-down electrons from the VB, generating spin-up electrons in the CB. Likewise, LCP photons can only excite spin-up electrons from the VB, generating spin-down electrons in the CB.

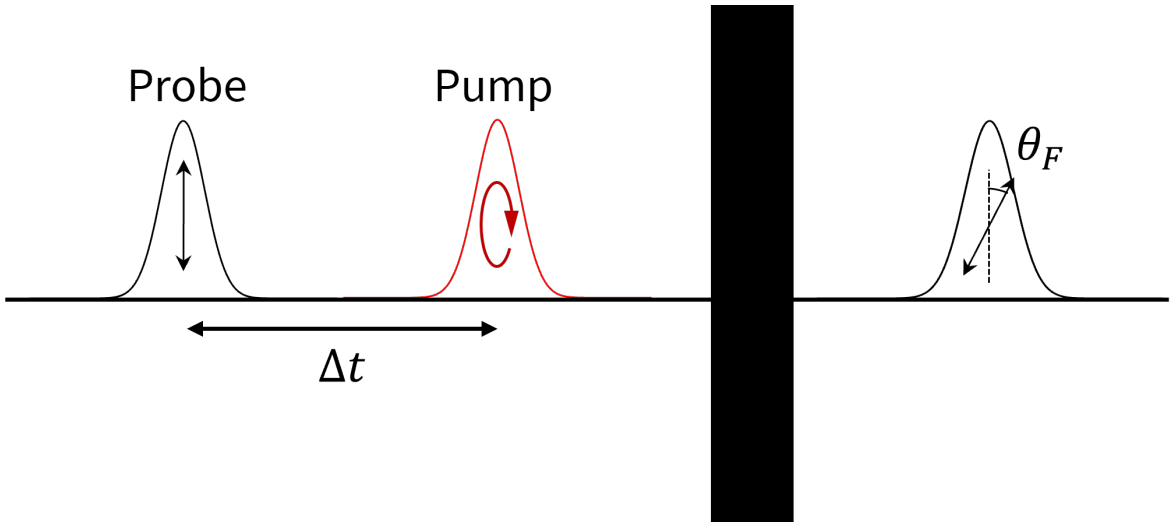

Figure 2.2 Illustration of the pump-probe dynamics on the sample. The pump and probe pulses are separated by a time delay Δt. The pump pulse spin polarizes the sample, while the probe pulse analyzes the spin polarization. The transmitted probe polarization is rotated by an angle proportional to the degree of spin polarization (exaggerated for clarity).

sample at a specific delay time. The strength of the carrier spin orientation is then analyzed for a given time after the pump polarized the sample. Thus, we measure the decay of the carrier spin polarization as a function of the pump-probe delay.

To further analyze the spin properties using this technique, the sample is placed in a magnet in transverse (Voigt) geometry, such that the magnetic field is applied perpendicular to the propagation of the incident light. The magnetic field disturbs the decay of the spin polarization, causing the net magnetic moment to precess. Then, the strength of the carrier spin orientation does not decay directly to 0; rather, it experiences oscillatory exponential decay to 0 as the magnetic field acts like a driving force. The frequency of these oscillations can be used to measure the strength of the spin-orbit coupling in the material. Furthermore, the decay time of the spin polarization measured using this setup gives the inhomogeneous spin decoherence time (T_2^*) of carriers in the material.

2.2.1 Experimental Setup

For the GaAs and $MAPbI_3$ samples, I tuned a pulsed Ti:Sapph laser to 821 nm and 800 nm respectively, aligned to their excitonic peaks. The pulses are ~100 fs long pulses emitted at an 86.7 MHz repetition rate.

The TRFR and TRKR experimental setups in our lab are depicted in Figures 2.3 and 2.4 respectively. Using a 90:10 beamsplitter, the pulses were separated into distinct pump and probe beams. The pump beam reflects 180° off a retroreflector placed on a delay stage. After the delay stage, the beam is reflected off several mirrors before transmitting through a linear polarizer oriented along the horizontal and a photoelastic modulator (PEM) with fast axis oriented at 45°. This circularly polarizes the pump pulse. Then, the pump is focused at a slight angle onto the center of our sample. It is important to tune the pump pulse intensity to optimize data collection because spin decoherence times typically decrease as the intensity increases. For GaAs, a power output of 25-30 mW was suitable for collecting reliable data. For $MAPbI_3$, the optimal decay times correspond to

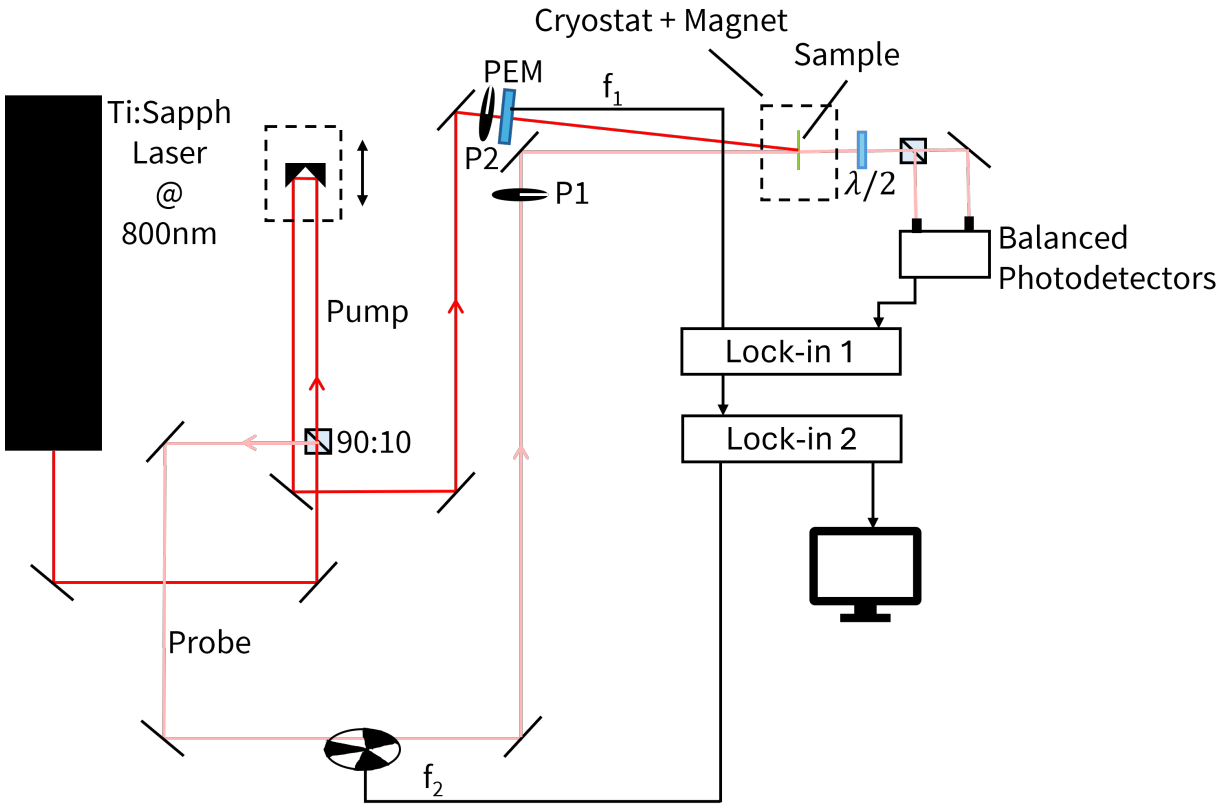

Figure 2.3 The experimental setup for time-resolved Faraday rotation (transmission geometry). The laser pulse output of the Ti:Sapph is split using a 90:10 beamsplitter into distinct pump (red) and probe (light red) beams. These beams are both maintained at the same wavelength. The beams are guided separately before being focused onto the sample such that their respective path lengths are relatively similar. The pump beam is modulated between RCP and LCP using a photoelastic modulator (PEM) with fast axis oriented at 45°, while the probe beam is modulated using a chopper. The probe beam is linearly polarized using polarizer P1 before the sample. A half-waveplate after the sample ($\lambda/2$) is used to balance the detectors with the pump beam blocked. The output of the photodetectors is read by lock-in 1 referenced to the PEM frequency. The output of lock-in 1 is read by lock-in 2, referenced to the chopper frequency.

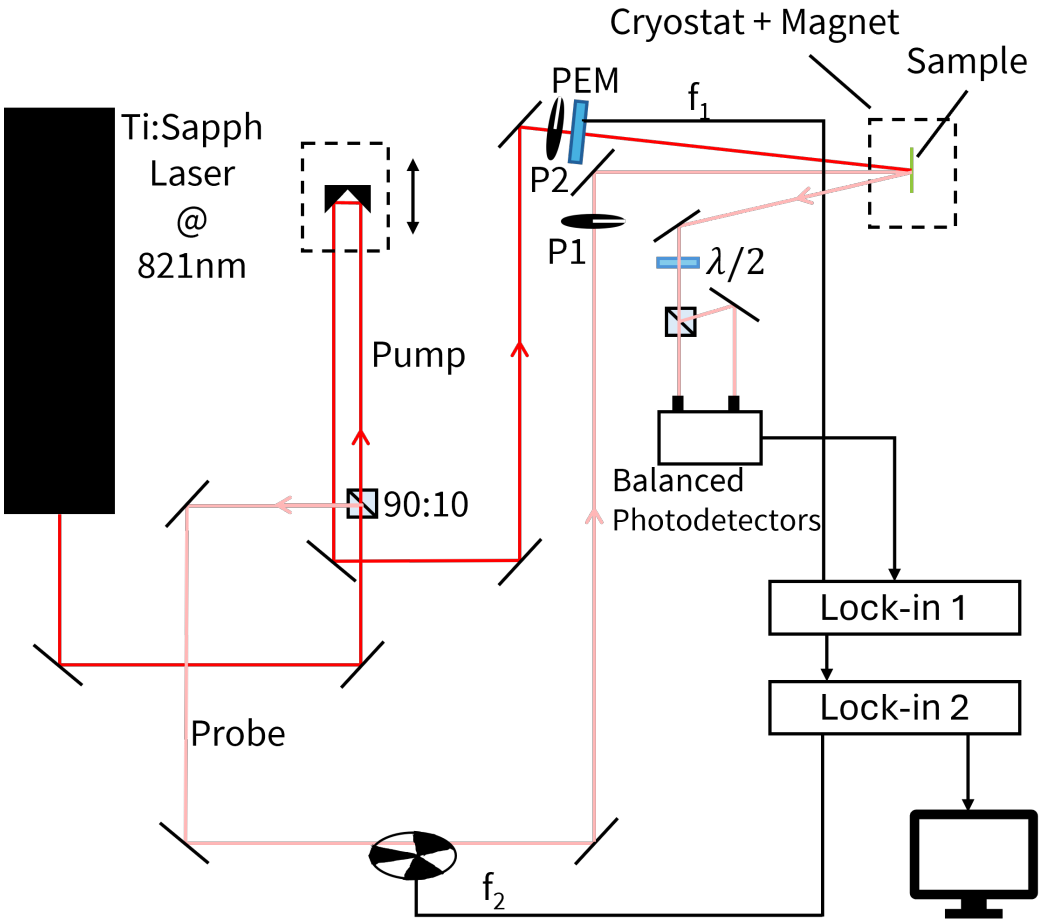

Figure 2.4 The experimental setup for time-resolved Kerr rotation (reflection geometry). The setup prior to the sample is identical to the setup in transmission geometry. The polarizing beamsplitter, half-waveplate, and balanced photodetectors are moved to the opposide side of the sample.

an intensity of 5 W/cm^2 [15]—which roughly corresponds to a pump power of 40 mW in the setup. Higher power outputs can still result in good data; however, high pump intensities can degrade the sample (especially in the case of $MAPbI_3$).

The probe pulse is carefully guided such that the optical path length of the pump and probe beams remains identical. The probe beam is reflected through a vertically oriented linear polarizer. Then, it is focused through the center of the pump beam spot on the sample. To maintain better signal-to-noise ratio, the probe is focused to a smaller spot than the pump, such that the probe impinges on the part of the sample most uniformly excited by the pump pulse. As seen in Figure 2.3, the transmitted probe pulse is reflected through a half waveplate[1], then split into two beams with horizontal and vertical polarizations respectively. Each beam is focused onto separate photodiodes in the balanced photodetector—which outputs the voltage difference between the signals from each photodiode. Before scans can be conducted, two variables must be optimized. First, the voltage generated via the light on each diode should be somewhere between 80-100 mV (with the chopper on) for optimal data. Second, the difference signal should be minimized with the pump beam blocked to reduce signal artifacts resulting from sample birefringence and eliminate the common mode noise. This is done by rotating the half waveplate until the difference signal is minimized.

For both samples, spin-polarization effects decay rapidly at high temperatures. Thus, the samples were placed in a closed-cycle He cryostat, bringing the sample to temperatures as low as 5 K. To measure the spin precession, the cryostat sits inside a Helmholtz coil magnet capable of generating magnetic fields of up to 1.36 T.

[1] In some cases, a quarter waveplate is used instead of the half waveplate. However, this is only necessary in the case that the sample exhibits circular dichroism (CD) i.e., that it preferentially absorbs more RCP than LCP light (or vice versa) [17]. If the CD is small relative to the phase shift (which rotates the linear polarization), then only the half waveplate is necessary. In the case of our samples, both GaAs and $MAPbI_3$ are achiral so a half waveplate is sufficient.

2.2.2 Double-lockin detection

To improve the signal-to-noise ratio, a double-lockin detection method was utilized. This requires two modulation schemes—the pump beam is modulated sinusoidally between RCP and LCP light using the PEM at 42.7 kHz, while the probe beam is modulated on and off using a chopper at 1200 Hz. The resulting difference signal output by the balanced photodetector should look similar to Figure 2.5. The first lockin is referenced to the PEM frequency. Then, the 'X' (or in-phase) component of the signal measured by the lockin is wired to the input of the second lockin. This signal looks similar to Figure 2.6. Because lockin 1 averages over the oscillations due to the PEM, it will output a square wave with non-zero amplitude which depends on the strength of the PEM oscillations. This square wave is modulated at the chopper frequency. Thus, lockin 2 is referenced to the chopper frequency, and the signal measured here corresponds to the TRFR/TRKR signal for a given time delay.

Several considerations must be taken into account when using a double-lockin detection scheme. First, the time constant of lockin 1 must be (1) shorter than half the period of the chopper modulation and (2) longer than the period of the PEM modulation. A good choice can be made using a geometric mean frequency. In my case, the period corresponding to the geometric mean is

$$T = \frac{1}{\sqrt{f_1 f_2}} = 0.140 \text{ ms},$$

so I set the time constant of lockin 1 to 100 μs. Additionally, since the X component of the lockin signal is output to lockin 2, it is necessary to optimize the phase of lockin 1 to maximize the X component (and minimize the Y component). Otherwise, lockin 1 may average over the signal at the edge between the non-zero and zero signals and deliver spurious data. Lastly, the sensitivity for lockin 1 should be set as large as possible without lockin 2 overloading. Typically, setting lockin 2 to "high reserve" can reduce the chance of it overloading if there are issues.

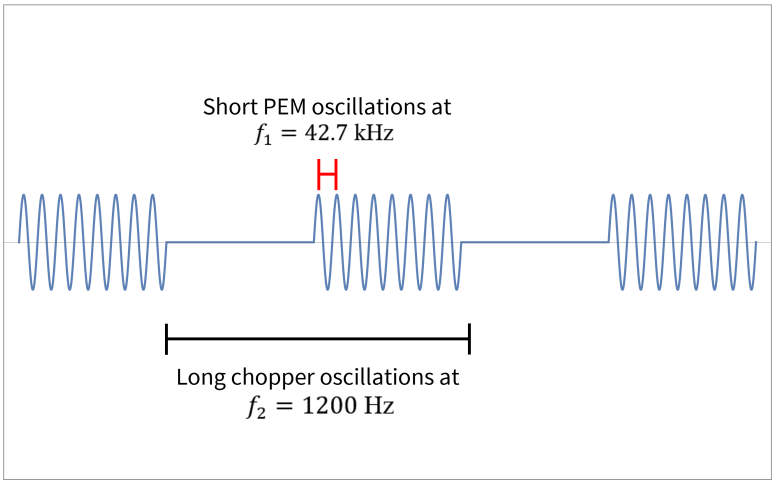

Figure 2.5 The voltage difference output by the balanced photodiodes. When the probe beam transmits through the chopper, signal can be observed, but only if there is sample spin polarization resulting from the pump beam. Thus, there are fast oscillations which correspond to the PEM modulation as well.

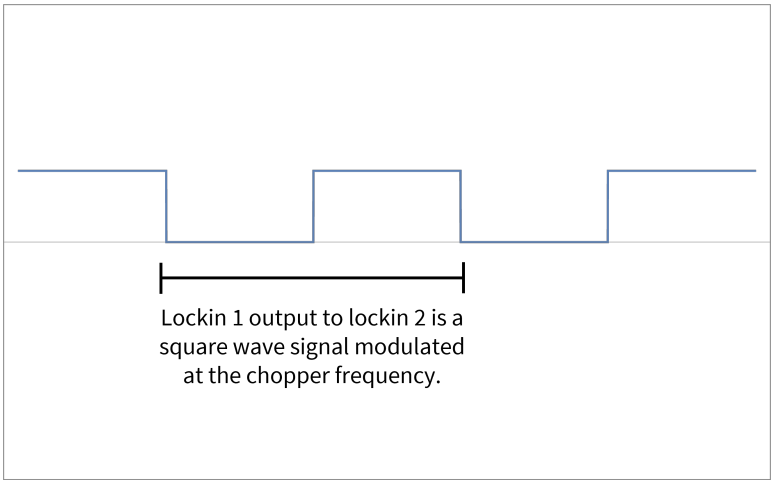

Figure 2.6 The signal output from lockin 1. The PEM oscillations were averaged over, resulting in a square wave output from lockin 1 to lockin 2. The amplitude of the oscillations determine the amplitude of the square wave. This square wave is modulated at the chopper frequency.

Chapter 3

Results & Discussion

3.1 GaAs/AlGaAs Heterostructure

Preliminary data was collected at $B = 300$ mT to demonstrate clear Faraday rotation from the n-GaAs/AlGaAs heterostructure. This data is pictured in Figure 3.1. The left plot depicts the Faraday rotation as a function of time delay (smoothed using a 7-point adjacent averaging function).

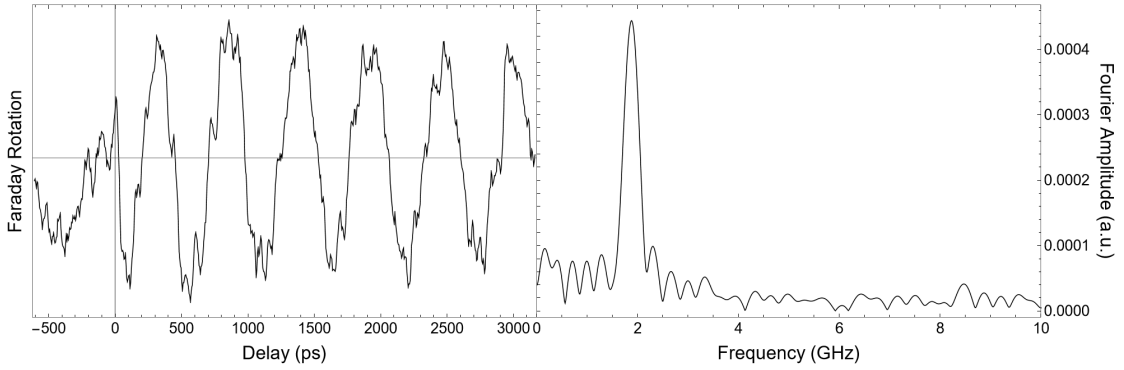

Figure 3.1 Data taken on GaAs/AlGaAs for $B = 300$ mT. On the left, the Faraday signal as a function of time delay is shown. Shown on the right is the Fourier transform of the time data, demonstrating a peak frequency of 1.880 GHz.

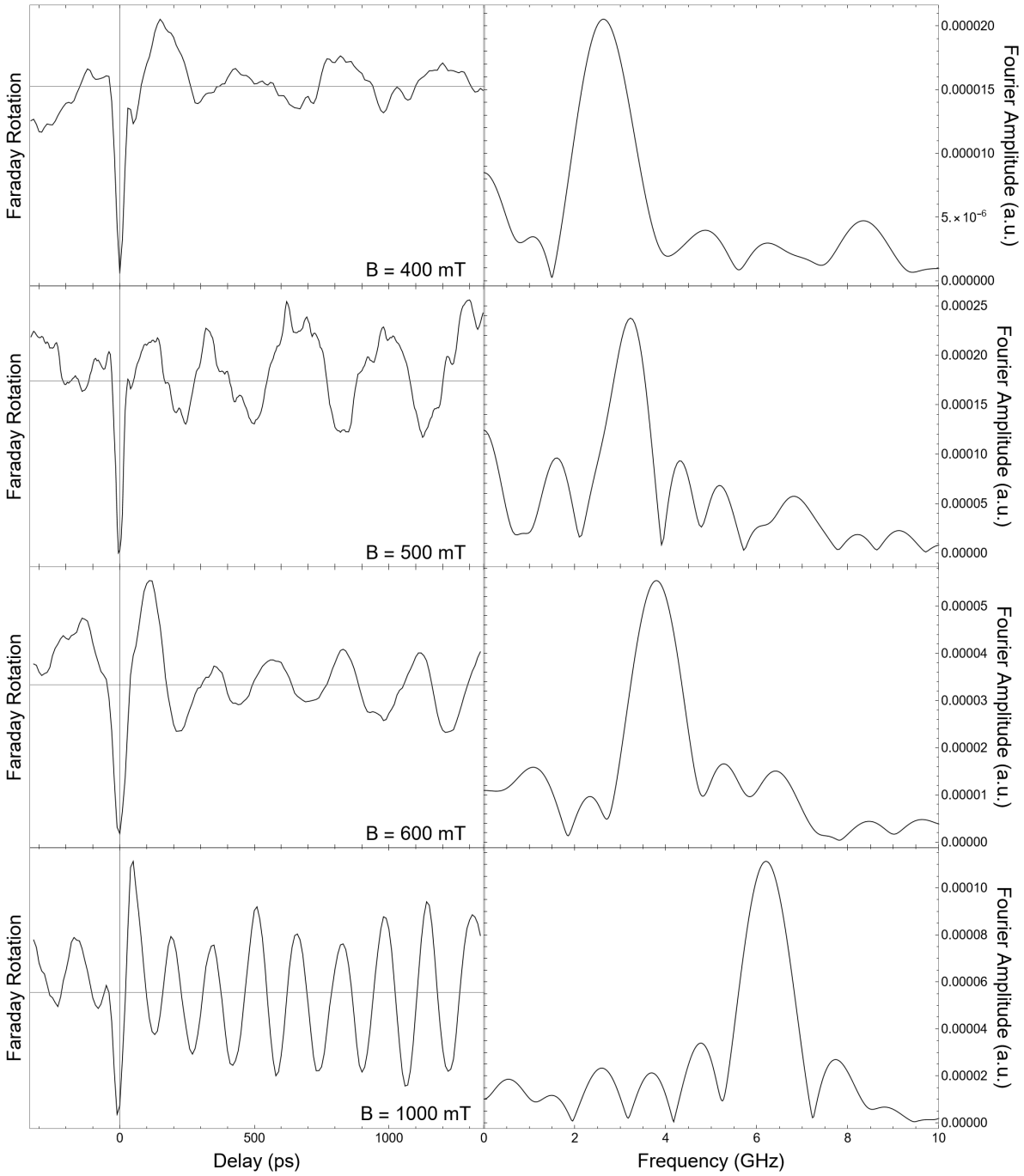

Figure 3.2 Data taken on GaAs/AlGaAs for various B-field strengths. On the left, the Faraday signal as a function of time delay is shown. Shown on the right is the Fourier transform corresponding to each field strength. Note that for higher fields, the Faraday rotation oscillates at higher frequencies. The data was taken for steps of 10 ps.

Because the GaAs sample has a long spin lifetime of 47 ns [18], the decay is not very pronounced. However, the data displays clear oscillations. From the right plot, which shows the Fourier transform of the raw data, there is a distinct frequency peak at 1.880 GHz. Given the relationship

$$hf = |g|\mu_B B, \tag{3.1}$$

the sample g-factor was calculated to be $|g| = 0.448$.

I then conducted a series of measurements at various magnetic field strengths. This data is pictured in Figure 3.2. The original data displayed an unwanted offset; I have corrected for it in the above plots to improve the accuracy of the Fourier transforms. Note that the data here was taken at longer time steps over a smaller time range. Hence, the frequency data included more noise than the previous data at 300 mT. For each magnetic field, I calculated the g-factor given Eq. 3.1 using the peak frequency, which is displayed in Table 3.1. The g-factors are plotted vs. frequency in Figure 3.3 and fit to a line, which gives the g-factor to be $|g| = 0.435 \pm 0.00860$. The fit's small r-squared value of 0.999 and low uncertainty indicates that the fitting parameter is very accurate.

Magnetic Field (mT)	Peak Frequency (GHz)	Frequency Uncertainty (GHz)	g-factor
300	1.880	$\pm$0.175	0.448
400	2.631	$\pm$0.695	0.470
500	3.223	$\pm$0.505	0.461
600	3.784	$\pm$0.635	0.451
1000	6.201	$\pm$0.598	0.443

Table 3.1 List of g-factors calculated from each set of magnetic field data

This result is in great agreement with previous data taken on this sample. Colton et. al. [18] measured its g-factor as $|g| = 0.42$ using a Hanle spin resonance experiment, which is very close to the measured value of $|g| = 0.435$, although not exactly identical. This indicates that my time-resolved Kerr rotation setup can reliably characterize the spin precession of the material's magnetic moment. While the results are not in perfect agreement, it is notable that the linear fit which assumes

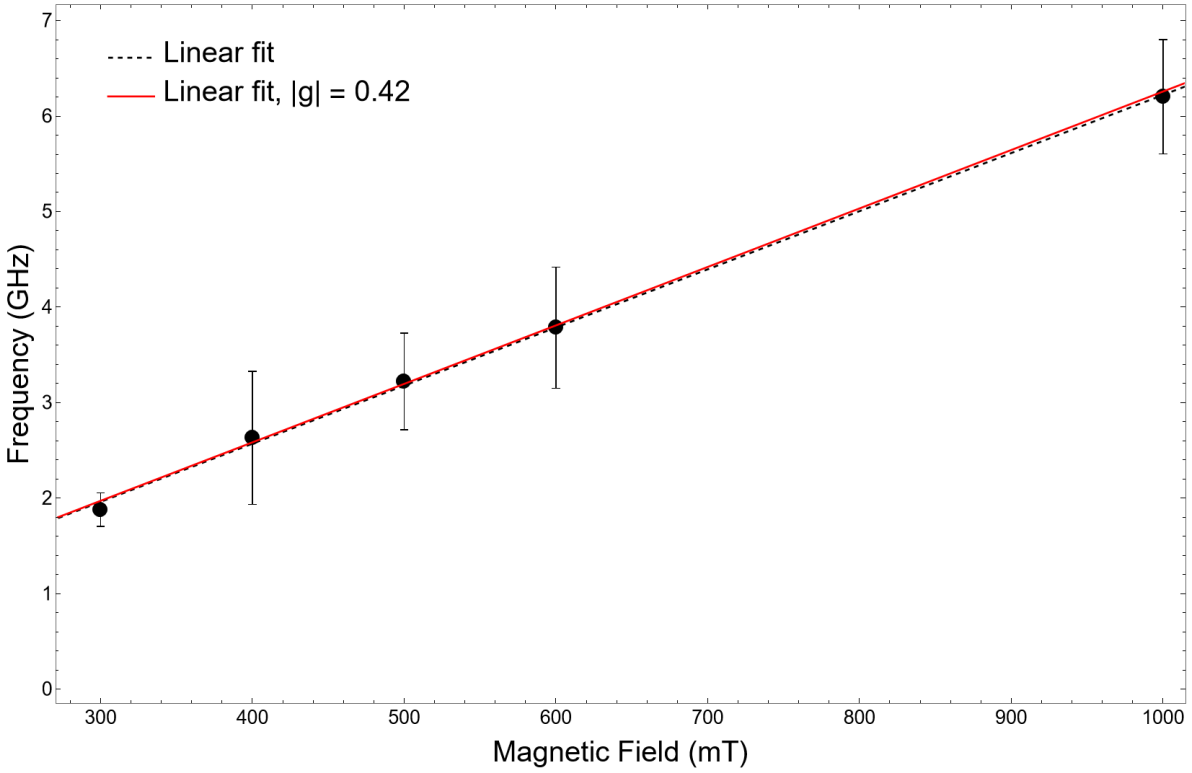

Figure 3.3 Plot of the frequency peaks as a function of the applied field. The frequency is proportional to the field strength by Eq. (3.1). Then, the slope of the plot is proportional to the g-factor of the heterostructure. The dashed fit is a typical linear model fit, whereas the red fit assumes the expected $|g| = 0.42$.

that $|g| = 0.42$ falls well within the error bars of each data point (see Figure 3.3). More precise measurements would likely bring the measured value closer to the expected value. There are three likely causes for the slight difference in the measured g-factor. First, as previously stated, the data taken at fields 400-1000 mT displayed an offset which I corrected for manually. Ideally, there would be no offset, which would improve the reliability of the Fourier transform. It is likely the offset arises from slight misalignments in the optics before the sample, so that the pump and probe are not perfectly aligned on top of each other at different delay times. Second, the 400-1000 mT data was taken at a non-ideal time step. To reduce noise in the Fourier transform, I would reduce the time step to fully resolve the oscillations and increase the lockin time constant. Finally, the frequency peaks in the Fourier transforms were broad; thus, collecting more oscillations by conducting longer scans would better resolve the frequency peaks and reduce the uncertainty.

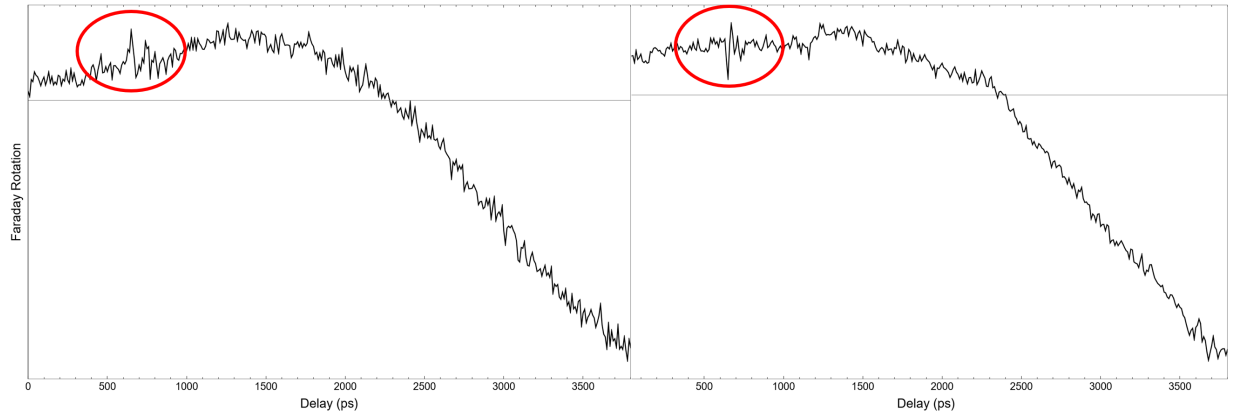

Figure 3.4 Raw data for $MAPbI_3$ over a long time period at two different intensities and zero field. Note the weird, long-range oscillation in the signal, which seems to indicate an alignment issue. However, there is still evidence that the alignment is close, from the fact a spike is observed at 650 ps in both scans (circled in red) where I expect that the pump and probe beams are aligned in time.

3.2 Methylammonium lead iodide

For $MAPbI_3$, the setup was swapped from reflection geometry to transmission geometry because the material is much less reflective than GaAs in the near infrared region. Based on a previous paper by Odenthal et al., we expect to observe two g-factors in $MAPbI_3$—$|g_h| = 2.63$ for holes and $|g_e| = 0.33$ for electrons—as well as a lifetime of 1,170 ps [15]. For various reasons, the data on methylammonium lead iodide is ambiguous and does not give clear indication of the spin lifetimes nor demonstrate oscillations in the presence of a magnetic field. In Figure 3.4, I display consistent data taken over long time periods. Interestingly, the signal exhibits long-range oscillations, which is unexpected for two reasons. First, the magnetic field was zero, so there should be no oscillations. Second, the oscillations occur over a large time period, whereas the period of oscillations for MAPI is much shorter. Thus, the data seems to indicate that faulty alignment may be affecting my results.

To investigate further, I narrowed the scan window to the area where peaks were observed near 650 ps. One sample set is plotted in Figure 3.5. There is a clear offset in the data. Furthermore, I

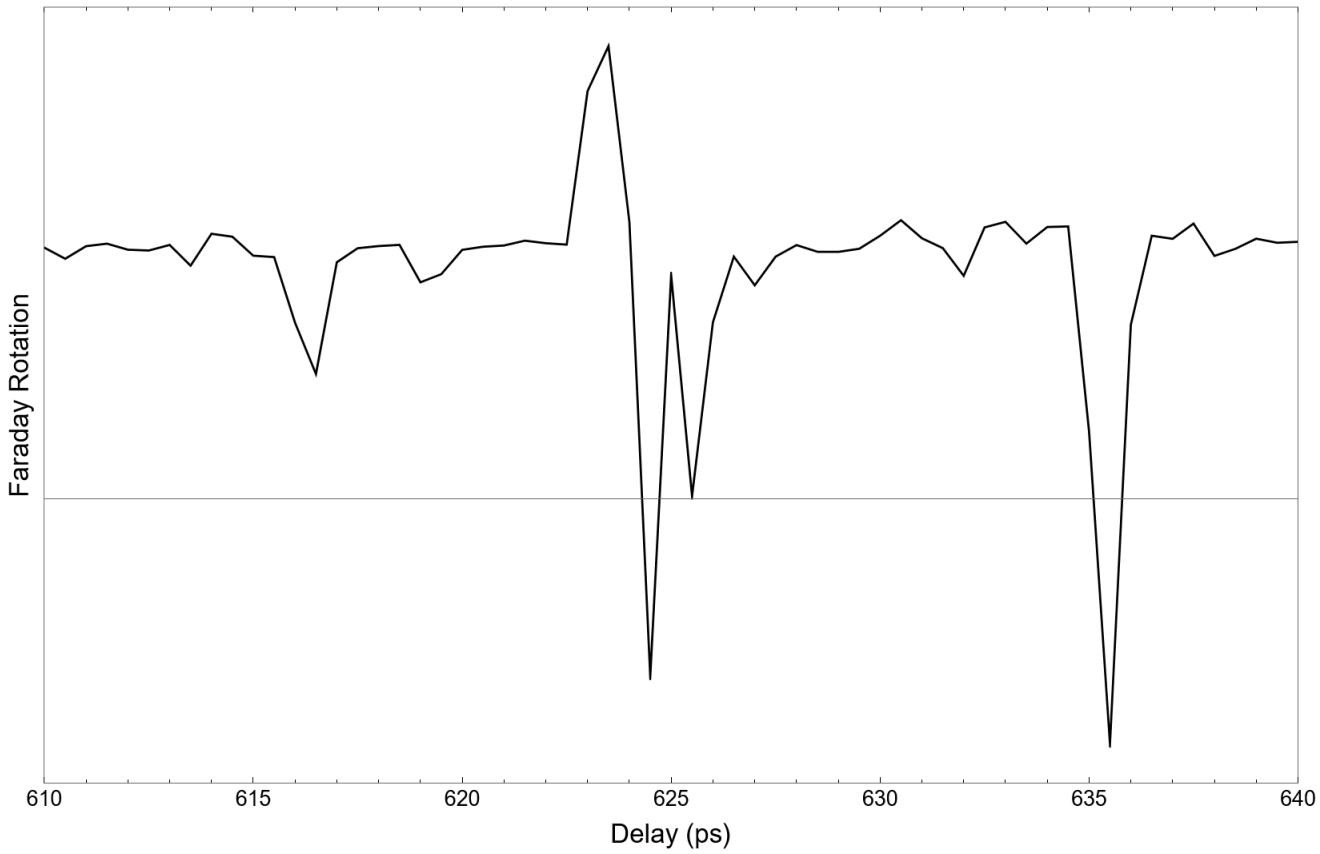

Figure 3.5 Raw data for MAPI from 610-640 ps with an incident power of 42 mW and $B = 500$ mT. The scan is relatively flat, apart from two sets of spikes at 625 ps and 635 ps. Both spikes are consistently there in all scans conducted at higher step resolution.

observe two spikes over the course of the scan—they could be attributed to noise, but both spikes appeared through other scans I conducted, so it is unlikely they arise from noise. It is likely that the first spike corresponds to the alignment of the pump and probe in time, while the second spike corresponds to a reflection from the cryostat windows or the back side of the glass substrate. This could affect my data negatively once I adjust and improve the optical alignment. Thus, to improve chances of observing real signal from $MAPbI_3$, it is necessary to adjust the optical alignment to remove the reflection as well.

Chapter 4

Conclusion

TRFR/TRKR is a versatile experiment that allows one to characterize the spin properties of non-magnetic materials—notably spin-orbit coupling (via the g-factor) and the inhomogeneous spin decoherence time T_2^*. In this paper, I demonstrated its use by testing a n-GaAs/AlGaAs heterostructure in reflection geometry. I clearly showed that the calculated g-factor agreed well with previous papers on the same sample and the expected g-factor fell well within the error bars. However, I failed to obtain any accurate data on $MAPbI_3$ after adjusting the setup for transmission geometry. Most likely, the data issues arise from optical misalignment of the pump beam that causes its position on the sample to move as time delay is scanned. It is unclear why I obtained great data on the GaAs sample but failed to observe anything on the $MAPbI_3$ sample.

Although I could calculate the g-factor of the GaAs sample, I was unable to measure the T_2^* time using my setup because the sample's decay time is 47 ns [18], much longer than the 3.88 ns resolvable in the current setup. However, once we can collect reliable data on $MAPbI_3$, we should observe a clear decay time, since the decay time is on the scale of 100-1000 ps [15].

To improve data collected on these samples, I suggest implementing several methods to troubleshoot and fix the current setup. First, it would be ideal to align the pump and probe beams in time and maximize the observed signal by tweaking the optics near the sample. If that fails to yield

good data, it is likely necessary to reduce the pump beam drift as the time delay is scanned by (1) improving the alignment of the translation stage or (2) telescoping the pump beam so that it is slightly defocused on the sample—such that even if the pump beam moves a little, the probe beam will still be aligned in the center of the pump beam. If all else fails, it may be prudent to maximize the signal using the Ti:Sapph in CW mode.

4.1 Future Plans

After collecting reliable data on $MAPbI_3$, we will test strained $MAPbI_3$ samples. Using samples synthesized using substrate clamping by Kelsey Garden at the University of Utah, we will test the effects of strain on $MAPbI_3$'s spin properties. The increased strain will break the crystal inversion symmetry further. We expect that this will increase the material's spin-orbit coupling strength. It is likely that it will also affect the T_2^* time. By tuning the induced strain, one can control the SOC strength, making it easier to optimize for spintronic applications. More information on this method is contained in Appendix A.

Beyond TRFR, we plan to incorporate additional experiments on these strained samples to fully characterize their spin properties. For example, although TRFR can measure the T_2^* time, this has limited usefulness; it includes the effect of inhomogeneities and defects within the material, which can differ dramatically from sample to sample [19]. However, it allows one to put a lower limit on the homogeneous spin decoherence time T_2 since T_2^* is always less than or equal to T_2. Other experimental methods are necessary to fully characterize the T_2 time. For instance, electron spin echo can measure the T_2 time by intentionally dephasing electrons and measuring the time it takes for electrons to become in-phase [19]. To further characterize the spin properties of $MAPbI_3$, it would be useful to measure its T_2 time using a spin echo experiment. Furthermore, a Hanle effect

measurement (a steady-state version of TRFR) can verify the g-factors calculated using TRFR and clarify the origin of the spin polarization response in the material.

Appendix A

Substrate clamping to induce biaxial strain

Substrate clamping offers an additional method for tuning sample properties during synthesis by inducing biaxial strain. In this method, the initial process for synthesizing $MAPbI_3$ is identical to the process given in Chapter 2. To maximize the induced strain, a substrate is chosen to have a mismatched coefficient of thermal expansion with $MAPbI_3$. The larger the difference, the more strain can be induced. Then, the sample is spin-coated on the substrate, annealed at 400°C for less than a second, and rapidly cooled. As seen in Figure A.1, the sample compresses perpendicular to the substrate plane. However, the in-plane compression is limited, inducing biaxial strain in the plane.

Unfortunately, the induced strain diminishes rapidly after synthesis. It can reduce to about 20% of its original value within hours. However, it generally retains about 20% of its original strain permanently [20].

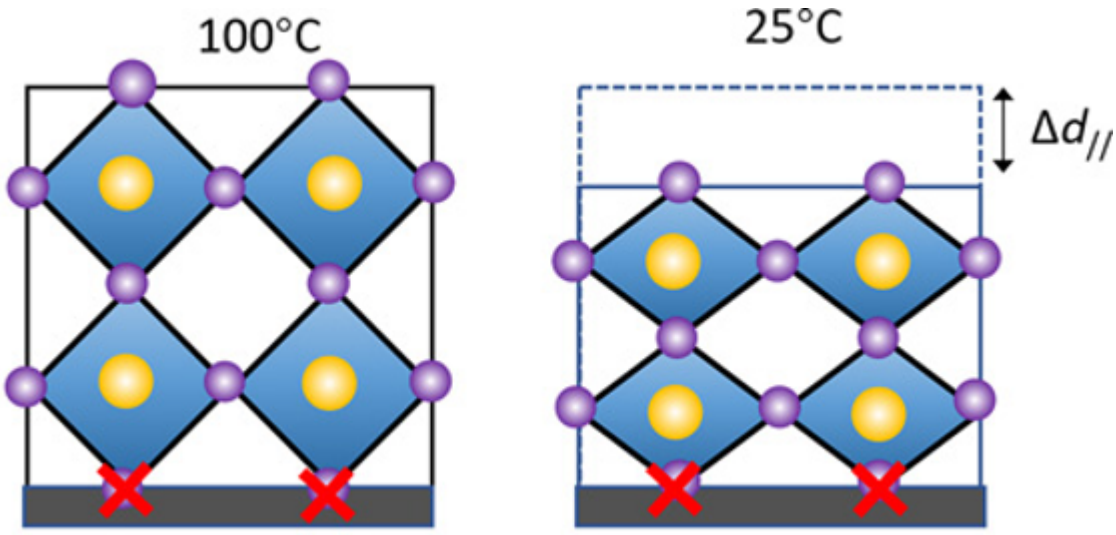

Figure A.1 Biaxial strain is induced using thermal mismatch between the substrate and the $MAPbI_3$ sample. With no substrate, the lattice can compress equally on all sides when cooling, so no strain is left within the material. When coated on a material with a different coefficient of thermal expansion, $MAPbI_3$ is compressed nonuniformly, resulting in strain throughout the structure. Figure adapted from [21].

Bibliography

[1] S. Datta and B. Das, "Electronic analog of the electro-optic modulator," Applied Physics Letters **56,** 665–667 (1990).

[2] S. Datta, "How we proposed the spin transistor," Nature Electronics **1,** 604–604 (2018).

[3] G. F. A. Malik, M. A. Kharadi, F. A. Khanday, and N. Parveen, "Spin field effect transistors and their applications: A survey," Microelectronics Journal **106,** 104924 (2020).

[4] D. Osintsev, V. Sverdlov, A. Makarov, and S. Selberherr, "Ballistic Transport Properties of Spin Field-Effect Transistors Built on Silicon and InAs Fins," ECS Transactions **39,** 155 (2011).

[5] C. Eames, J. M. Frost, P. R. F. Barnes, B. C. O'Regan, A. Walsh, and M. S. Islam, "Ionic transport in hybrid lead iodide perovskite solar cells," Nature Communications **6,** 7497 (2015).

[6] Moving Wannier exciton, "Exciton — Wikipedia, The Free Encyclopedia,", 2008, [Online; accessed 28-March-2025].

[7] K. W. Böer and U. W. Pohl, in *Semiconductor Physics* (Springer International Publishing, Cham, 2018), pp. 485–525.

[8] S. B. Nam, D. C. Reynolds, C. W. Litton, R. J. Almassy, T. C. Collins, and C. M. Wolfe, "Free-exciton energy spectrum in GaAs," Phys. Rev. B **13,** 761–767 (1976).

[9] J. Even, L. Pedesseau, and C. Katan, "Analysis of Multivalley and Multibandgap Absorption and Enhancement of Free Carriers Related to Exciton Screening in Hybrid Perovskites," The Journal of Physical Chemistry C **118,** 11566–11572 (2014).

[10] Y. Yamada, T. Nakamura, M. Endo, A. Wakamiya, and Y. Kanemitsu, "Photoelectronic Responses in Solution-Processed Perovskite CH_3 NH_3PbI_3 Solar Cells Studied by Photoluminescence and Photoabsorption Spectroscopy," IEEE Journal of Photovoltaics **5,** 401–405 (2015).

[11] Y. Yang, D. P. Ostrowski, R. M. France, K. Zhu, J. van de Lagemaat, J. M. Luther, and M. C. Beard, "Observation of a hot-phonon bottleneck in lead-iodide perovskites," Nature Photonics **10,** 53–59 (2016).

[12] R. Winkler, "Spin–orbit coupling in solids," in *Encyclopedia of Condensed Matter Physics (Second Edition)*, T. Chakraborty, ed., (Academic Press, 2024), pp. 186–192.

[13] J. Atulasimha and S. Bandyopadhyay, *Nanomagnetic and Spintronic Devices for Energy-Efficient Memory and Computing* (John Wiley & Sons, Incorporated, Newark, United Kingdom, 2016).

[14] G. Dresselhaus, "Spin-orbit coupling effects in zinc blende structures," Physical Review **100,** 580 – 586 (1955).

[15] P. Odenthal, W. Talmadge, N. Gundlach, R. Wang, C. Zhang, D. Sun, Z.-G. Yu, Z. V. Vardeny, and Y. S. Li, "Spin-polarized exciton quantum beating in hybrid organic–inorganic perovskites," Nature Physics **13,** 894–899 (2017).

[16] J. Colton, T. Kennedy, A. Bracker, and D. Gammon, "Spin Lifetime Measurements in MBE-Grown GaAs Epilayers," physica status solidi (b) **233,** 445–452 (2002).

[17] J. Hubner and M. Oestreich, "Time-Resolved Spin Dynamics and Spin Noise Spectroscopy," in *Spin Physics in Semiconductors*, M. I. Dyakonov, ed., (Springer-Verlag Berlin Heidelberg, 2008), Chap. 5, pp. 115–134.

[18] J. S. Colton, T. A. Kennedy, A. S. Bracker, J. B. Miller, and D. Gammon, "Dependence of optically oriented and detected electron spin resonance on donor concentration in *n*-GaAs," Solid State Communications **132,** 613–616 (2004).

[19] K. Miller, Bachelor's thesis, Brigham Young University, 2015.

[20] Z. Zhang, 2025, private communication.

[21] J. Zhao, Y. Deng, H. Wei, X. Zheng, Z. Yu, Y. Shao, J. E. Shield, and J. Huang, "Strained hybrid perovskite thin films and their impact on the intrinsic stability of perovskite solar cells," Science Advances **3,** eaao5616 (2017).